Atomization and Sprays, 27(1): 61–79 (2017)

ASSESSMENT OF DROPLET BREAKUP MODELS IN HIGH-SPEED CROSS-FLOW

Anand Bhandarkar, P. Manna, & Debasis Chakraborty*

Defence Research and Development Laboratory, Kanchanbagh, Hyderabad-500058, India

*Address all correspondence to: Debasis Chakraborty, Defence Research and Development Laboratory, Kanchanbagh, Hyderabad-500058, India, E-mail: debasis_cfd@drdl.drdo.in

Original Manuscript Submitted: 9/10/2015; Final Draft Received: 5/14/2016

The breakup process in quiescent atmosphere and high-speed cross-flow is numerically simulated. Three-dimensional RANS equations with the K-ε turbulence model are solved using commercial CFD software. Different droplet breakup models, namely, TAB, ETAB, Ritz-Diwakar, and KH-RT models are studied to assess their predictive capability in characterizing spray in high-speed cross-flow. The validation test cases include liquid injection into quiescent atmosphere, and subsonic and supersonic cross-flow. Computed droplet velocity, droplet size, and spray penetration are compared with the experimental/numerical data available in the literature. For diesel injection in quiescent atmosphere, computed spray penetration matches reasonably well with the experimental data. For subsonic cross-flow, although the penetration height is underpredicted, SMD distribution and particle velocity match reasonably well with the experimental data. The ETAB model captures the SMD values at different locations and velocities better with experimental data in comparison to the TAB model. For the supersonic cross-flow case, penetration height and SMD have a good match with the experimental data. The Stokes drag model performs better than the high-Mach and dynamic drag models. Droplet drag law for supersonic flow needs to be revised to have better predictive capability of spray characteristics in high-speed flow.

KEY WORDS: *droplet breakup, high-speed cross-flow, CFD, SMD, particle velocity*

1. INTRODUCTION

Modeling of liquid atomization is important in various engineering applications including aerospace propulsion systems, automotive engines, food processing, inkjet printing, etc. For liquid fuel combustion such as rocket engine, automotive engines, and industrial furnaces, the fuel spray characteristics are critical to determine the engine performance such as combustion efficiency, fuel consumption rate, exhaust emissions.

Turbulent spray includes multiscale physical processes. In the liquid core region, the dense liquid column is affected by aerodynamic interaction causing instability of liquid surface and creating ligaments. The breakup process starts at the liquid jet surface by stripping liquid fragments and forming liquid droplets (primary breakup). This instability at the jet surface led to the formation of acceleration waves which deform and flatten the liquid column. The liquid column eventually disintegrates into ligaments and the droplets form sprays (secondary breakup). The final droplet production is greatly dependent on primary breakup, but it is difficult to know what is actually occurring in the primary breakup region.

Jet inertial and aerodynamic forces along with surface tension play an important role in ligament and droplet formation. Several parameters such as momentum flux ratios, Weber number, and Ohnesorge number are also very important in droplet breakup process.

Experimentally, observation of this dense and small region with high spatiotemporal resolution is extremely difficult. Masutti et al. (2009) depicted the flow features of the jet breakup process in the presence of high-speed cross-flow which is reproduced in Fig. 1. The dynamic force of the air cross-flow causes the jet to flatten and bend towards the direction of the air stream. The clumps and ligaments that are formed undergo secondary atomization.

1044–5110/17/$35.00

NOMENCLATURE

a	radius of parent parcel	u	velocity
a_p	acceleration of droplet	We	Weber number
A	droplet surface area	Z	Ohnesorge number
B_o	model coefficient for droplet size		
C_c	Cunningham correction factor	**Greek Symbols**	
C_d	drag coefficient	ρ	density
$C_{d,sphere}$	drag coefficient of sphere	λ	thermal conductivity
C_L	Levich constant (i.e., 5.7)	δ	molecular mean free path
C_p	specific heat	τ_{ik}	turbulent shear stress
d	particle diameter	μ	dynamic viscosity
dm_p/dt	rate of evaporation	τ	breakup time
d_o	reference nozzle diameter	Λ	wavelength of most unstable wave
F_D	drag force	Ω	growth rate of most unstable wave
h	convective heat transfer coefficient	τ_{RT}	frequency of the fastest growing wavelength of R-T wave
h_{fg}	latent heat		
H	total energy	σ	liquid surface tension
m	mass		
P	pressure		
Pr	Prandtl number	**Subscripts**	
r	droplet radius	l	liquid phase
r_{stable}	new radius for the stable droplet	g	gas phase
R	universal gas constant	L	laminar
Re	Reynolds number	T	turbulent
S	Sutherland constant	ref	reference value
S_h	energy source term	p	particle phase
S_m	mass source term	∞	continuous phase
t_{br}	characteristic breakup time	KH	K-H wave
T	temperature, also Taylor number	RT	R-T wave

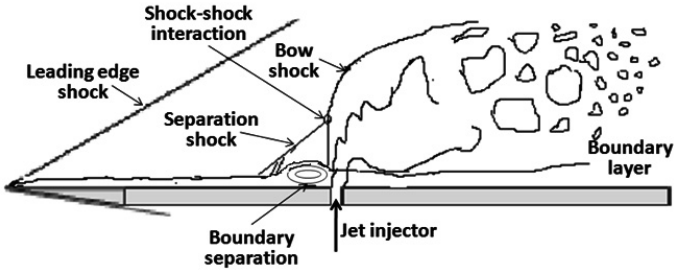

FIG. 1: General flow topology of jet injection in compressible crossflow

Droplet stripping from the jet sides may also occur before the point of column fracture. The appearance of a separation shock and separation bubble further forces the liquid jet to mix with the air upstream of the injection under subsonic conditions. Column breakup and the surface breakup are two basic mechanisms of formation of droplets.

Several experimental studies (Wu et al., 1995, 1997; Kitamura and Takahashi, 1996; Lin et al., 2004; Schetz and Padhye, 1977) are reported to analyze the primary breakup region to understand its physics. Kitamura and Takahashi (1996) showed that decrease in the jet to the cross-flow momentum flux ratio caused a decrease in breakup length. So far, the entire physics has not been unveiled by experiments and further efforts are continuing.

Numerical simulations are also performed to explain droplet breakup phenomena. Because of the severe resolution requirement for high Weber and Reynolds numbers, it is difficult to simulate the primary breakup phenomena accurately. Among the existing atomization models, the Kelvin-Helmholtz instability model of Reitz (1987) (BLOB model) and the Taylor analogy breakup (TAB) model of O'Rourke and Amsden (1987) remain very popular because of their easy implementation in multidimensional CFD solvers. Different modifications of these models, namely, ETAB of Tanner (1997, 2003), the cavitation model of Nishimura and Assanis (2000), etc., are also applied to study different atomization processes in spray modeling. Trinh and Chen (2006) included the effect of turbulence in the BLOB and TAB models to study the effect of primary and secondary breakup. Balasubramanyam and Chen (2008) incorporated the finite-conductivity spray evaporation model and improved drag coefficient correlation to study liquid jet breakup in high-speed flow.

Yang et al. (2009) performed three-dimensional large eddy simulation (LES) to simulate the experimental conditions of Stenzler et al. (2003). Although computed spray penetration depth matches reasonably well with experimental data for several variants of liquid-gas momentum flux ratio; computed SMD distributions differ. Wang and Rutland (2003) have performed two-dimensional direct numerical simulation (DNS) in the Eulerian-Lagrangian framework using the S3D code (Kennedy and Carpenter, 1994) of Sandia National Laboratory. Different submodels of droplet such as the breakup model, distortion model, evaporation model, collision model, etc., were validated and their effect on the turbulence structure of isotropic flow was investigated. Since DNS and LES studies require submicron and picosecond level of spatial and temporal resolution to predict the atomizing sprays in high-velocity cross-flows, their applications in practical engineering problems are very limited. Hence, the engineering analysis and design of liquid spray devices still rely on the phenomenological engineering model. However, before putting these models in a design exercise, it is necessary to validate different simplifying assumptions by comparing them with reliable experimental data. A validated model will lead to better predictions of spray characteristics such as initial droplet size distribution, spray angle, and jet structure. In the present work, the predictive capabilities of different phenomenological engineering models available in the commercial CFD software were assessed to predict droplet breakup characteristics in three different flow regimes, namely, (1) in quiescent atmosphere, (2) in the presence of subsonic cross–flow, and (3) in the presence of supersonic cross-flow. Simulations are performed using CFX 14.4 (2012) with TAB, ETAB, and RD models for the quiescent atmosphere and subsonic cross-flow test cases; while the KH-RT model is used for supersonic cross-flow test cases with Fluent 14.5 (2012).

2. ANALYSIS

2.1 Governing Equations

The system of governing equations describing the conservation of mass, momentum, energy, and species transport equations of compressible gas flows are written as

Conservation of Mass equation:

$$\frac{\partial \rho}{\partial t} + \frac{\partial}{\partial x_l}(\rho u_l) = S_m; \quad l = 1,\, 2,\, 3. \tag{1}$$

The source S_m is the mass added to the continuous phase from the dispersed second phase (for example, due to vaporization of liquid droplets).

Conservation of Momentum equation:

$$\frac{\partial}{\partial t}(\rho u_i) + \frac{\partial}{\partial x_l}(\rho u_i u_l) + \frac{\partial P}{\partial x_i} = \frac{\partial(\tau_{il})}{\partial x_l} + F_i, \quad i,\, l = 1, 2,\, 3, \tag{2}$$

where $P = \rho RT$, τ is the turbulent shear stress, and F is the external body forces (arising from interaction with the dispersed phase).

Conservation of Energy equation:

$$\frac{\partial}{\partial t}(\rho H) + \frac{\partial}{\partial x_l}(\rho u_l H) = -\frac{\partial (u_j \tau_{jl})}{\partial x_l} + \frac{\partial q_l}{\partial x_l} + S_H, \quad j, l = 1, 2, 3, \tag{3}$$

where total energy ($H = C_p T$) and energy sources (S_H) include heat transfer between the continuous and the discrete phase. Properties of air are varied with temperature. The heat flux q_l is calculated as $q_l = -\lambda \partial T / \partial x_l$; λ is the thermal conductivity.

2.2 Turbulence Transport Equations (K-ε Turbulence Model)

Turbulent kinetic energy (k) equation:

$$\frac{\partial}{\partial t}(\rho k) + \frac{\partial}{\partial x_l}(\rho u_l k) = \frac{\partial}{\partial x_l}\left[\left(\frac{\mu_L}{\mathrm{Pr}} + \frac{\mu_T}{\sigma_k}\right)\frac{\partial k}{\partial x_l}\right] + S_k. \tag{4}$$

Turbulent eddy dissipation (ε) equation:

$$\frac{\partial}{\partial t}(\rho \varepsilon) + \frac{\partial}{\partial x_l}(\rho u_l \varepsilon) = \frac{\partial}{\partial x_l}\left[\left(\frac{\mu_L}{\mathrm{Pr}} + \frac{\mu_T}{\sigma_\varepsilon}\right)\frac{\partial \varepsilon}{\partial x_l}\right] + S_\varepsilon, \tag{5}$$

where $\mu = \mu_L + \mu_T$ is the total viscosity; μ_L, μ_T being the laminar and turbulent viscosity and Pr is the Prandtl number. The source terms S_k and S_ε of the k and ε equation are defined as

$$S_k = \tau_{il}\frac{\partial u_i}{\partial x_l} - \rho\varepsilon \quad \text{and} \quad S_\varepsilon = C_{\varepsilon 1}\tau_{il}\frac{\partial u_i}{\partial x_l} - C_{\varepsilon 2}\frac{\rho\varepsilon^2}{k},$$

where turbulent shear stress is defined as

$$\tau_{il} = \mu_T\left(\frac{\partial u_i}{\partial x_l} + \frac{\partial u_l}{\partial x_i}\right). \tag{6}$$

Laminar viscosity (μ_L) is calculated from Sutherland law as

$$\mu_L = \mu_{ref}\left(\frac{T}{T_{ref}}\right)^{3/2}\left(\frac{T_{ref} + S}{T + S}\right), \tag{7}$$

where T is the temperature and μ_{ref}, T_{ref}, and S are known coefficients. The turbulent viscosity μ_T is calculated as

$$\mu_T = C_\mu \frac{\rho k^2}{\varepsilon}. \tag{8}$$

The coefficients involved in the calculation of turbulent viscosity (μ_T) are taken from Launder and Spalding (1972) as

$$C_\mu = 0.09, \;\; C_{\varepsilon 1} = 1.44, \;\; C_{\varepsilon 2} = 1.92, \;\; \sigma_k = 1.0, \;\; \sigma_\varepsilon = 1.3, \;\; \sigma_c = 0.9.$$

2.3 Particle Trajectory Calculation

The particle transport model is capable of modeling dispersed phases which are discretely distributed in a continuous phase. The modeling involves separate calculation of each phase with source terms generated to account for the effects of the particles on the continuous phase. In this approach, the continuous phase is modeled in an Eulerian framework. In the dispersed phase, each particle interacts with the fluid and other particles discretely. The dispersed phase can exchange momentum, mass, and energy with the fluid phase. The most widely applied method available to determine the behavior of the dispersed phase is to track several individual particles through the flow field. Each

particle represents a sample of particles that follow an identical path. The behavior of the tracked particles is used to describe the average behavior of the dispersed phase. The force balance equates the particle inertia with the forces acting on the particle and can be written as

$$\frac{du_p}{dt} = F_D\left(\vec{u} - \vec{u}_p\right) + \frac{\vec{g}\left(\rho_p - \rho\right)}{\rho_p} + \vec{F} \tag{9}$$

where F_D is drag force per unit mass acting on the particle and F incorporates additional forces that can be important depending on application such as buoyancy force, forces due to domain rotation, virtual mass force, pressure gradient force, etc. Integration of time in the above equation yields the velocity of the particle at each point along the trajectory and the trajectory itself is predicted by

$$\frac{dx}{dt} = u_p \tag{10}$$

2.4 Heat Transfer to the Droplet

The heat transfer from the continuous phase to the discrete phase is computed by examining the change in thermal energy of a particle as it passes through each control volume. The droplet temperature is updated according to a heat balance that relates the sensible heat change in the droplet to the convective and latent heat transfer between the droplet and the continuous phase.

$$m_p c_p \frac{dT_p}{dt} = hA_p\left(T_\infty - T_p\right) - \frac{dm_p}{dt} h_{fg} \tag{11}$$

where $C_p =$ droplet heat capacity (J/kg·K), $T_p =$ droplet temperature (K), $h =$ convective heat transfer coefficient (W/m^2·K), $T_\infty =$ temperature of continuous phase (K), $dm_p/dt =$ rate of evaporation (kg/s), and $h_{fg} =$ latent heat (J/kg).

For high vaporization rates, the effect of the convective flow of the evaporating material from the droplet surface to the bulk gas phase becomes important. The convection/diffusion controlled evaporation model is used following the work of Miller et al. (1998) and Sazhin (2006) to calculate the rate of evaporation,

$$\frac{dm_p}{dt} = k_c A_p \rho_\infty \ln\left(1 + B_m\right) \tag{12}$$

where $k_c =$ mass transfer coefficient (m/s) and B_m is the Spalding mass number given by

$$B_m = \frac{Y_{i,s} - Y_{i,\infty}}{1 - Y_{i,s}},$$

where $Y_{i,s} =$ vapor mass fraction at the surface and $Y_{i,\infty} =$ vapor mass fraction in the bulk gas. The mass transfer coefficient k_c is calculated from the Sherwood number correlation given by Ranz and Marshall (1952).

2.5 Droplet Breakup Model

For the numerical simulation of droplet breakup, the statistical breakup approach is used. In this framework, it is assumed that if a droplet breaks up into child droplets, the particle diameter decreases. The particle number rate is adjusted so that the total particle mass remains constant (mass of parent droplet = mass of child droplets). Using this assumption, it is not required to generate and track new droplets after breakup, but to continue to track a single representative particle.

The Taylor analogy breakup (TAB) model is a classic method for calculating droplet breakup, which is applicable to many engineering sprays. The TAB model by O'Rourke and Amsden (1987) is based on an analogy between an oscillating and distorting droplet and a spring-mass system. The restoring force of the spring is analogous to the surface tension forces. The external force on the mass is analogous to the gas aerodynamic force. The damping forces

due to liquid viscosity are introduced to this analogy. The enhanced TAB model (ETAB) by Tanner (2003) uses the same droplet deformation mechanism as the standard TAB model, but uses a different relation for the description of the breakup process. It is assumed that the rate of child droplet generation is proportional to the number of child droplets.

The breakup model (RD model) of Reitz and Diwakar (1987) distinguishes between two breakup regimes: bag breakup and stripping breakup. Breakup occurs when the particle Weber number exceeds the critical value (called critical Weber number). The primary and secondary breakup is modeled using a linear stability analysis for liquid jets. This method is capable of predicting the intact core length as well as various regimes of breakup due to the action of different combination of liquid inertia, surface tension, and aerodynamic forces on the jet. The limitations include one characteristic size dimension for blob and the inability to predict drop size distribution and time between breakups. Independent of the breakup regime, it is assumed that during breakup the following relation describes the reduction of the particle radius,

$$\frac{dr_p}{dt} = -\frac{(r_p - r_{stable})}{t_{br}}, \tag{13}$$

where r_p is the droplet radius prior to breakup, r_{stable} is the new radius for the stable droplet, and t_{br} is the characteristic breakup time.

The KH-RT breakup model (Patterson and Reitz, 1999) combines the effects of Kelvin-Helmholtz waves driven by aerodynamic forces with Rayleigh-Taylor instabilities due to acceleration of shed drops ejected into free-stream conditions. The model assumes that a liquid core exists in the near-nozzle region. Child droplets are shed from this liquid core and are subjected to sudden acceleration when they are ejected into the free stream and Rayleigh-Taylor instability becomes the dominant effect. The length of the liquid core is obtained from Levich (1962) theory,

$$L = C_L d_0 \sqrt{\frac{\rho_l}{\rho_g}}, \tag{14}$$

where C_L is the Levich constant (i.e., 5.7) and d_o is a reference nozzle diameter. In the K-H mode, the model postulates that the radius of the newly-formed droplets (r) is proportional to the wavelength of the fastest-growing unstable surface wave on the parent parcel with radius, a, such that

$$r = B_o \Lambda_{KH}. \tag{15}$$

B_o is a model constant for droplet size and equal to 0.61 based on the work of Rietz (1987). Λ_{KH} is the wavelength corresponding to the most unstable K-H wave given by the dispersion relationship. This relation is derived from the linearized hydrodynamics equations for the liquid and gas and is given as follows,

$$\frac{\Lambda_{KH}}{a} = 9.02 \frac{\left(1 + 0.45Z^{0.5}\right)\left(1 + 0.4T^{0.7}\right)}{\left(1 + 0.87\mathrm{We}_g^{1.67}\right)^{0.6}}, \tag{16}$$

where Z is the Ohnesorge number and $T = Z\sqrt{\mathrm{We}_g}$ is the Taylor number. During the breakup, the parent parcel reduces in diameter due to the mass stripped from the parent parcel surface. Thus, the rate of change of the droplet radius in a parent parcel is given by

$$\frac{da}{dt} = -\frac{(a - r)}{\tau}, \tag{17}$$

where τ is the breakup time defined as $\tau = 9.02[(3.726B_1 r)/(\Lambda_{KH}\Omega_{KH})]$.

The B_1 is a breakup time constant which determines how quickly the parcel will lose mass. Therefore, a larger number means that it takes longer for the particle to lose a given amount of mass. A larger number for B_1 in the context of interaction with the gas phase would mean that the interaction with the subgrid is less intense. The breakup time constant, B_1, is set to a value of 1.73 as recommended by Liu et al. (1993). Values of B_1 can range between 1 and 60, depending on the injector characterization. Ω_{KH} is a growth rate corresponding to the most unstable wave, which is given by

$$\Omega_{KH}\left(\frac{\rho_l a^3}{\sigma}\right)^{0.5} = \frac{\left(0.34 + 0.38\mathrm{We}_g^{1.5}\right)}{(1 + Z)\left(1 + 1.4T^{0.6}\right)}. \tag{18}$$

The R-T breakup model also determines when and how droplets will break up by predicting the fastest growing disturbances. The fastest growing wavelength, Λ_{RT}, is given by

$$\Lambda_{RT} = 2\pi C_1 \sqrt{\frac{3\sigma}{a_p\left(\rho_l - \rho_g\right)}}, \tag{19}$$

where a_p is the acceleration of the droplet and C_1 is an adjustable constant depending on nozzle conditions. The associated breakup time scale, calculated from the frequency of the fastest growing wavelength, is given by

$$\tau_{RT} = \sqrt{\frac{\sigma^{0.5}\left(\rho_l + \rho_g\right)}{2}\left(\frac{3}{a_p\left(\rho_l - \rho_g\right)}\right)^{1.5}}. \tag{20}$$

When enough time has been passed, the breakup is allowed to occur. The radius of the newly formed parcel is defined as

$$r = 0.5\Lambda_{RT}. \tag{21}$$

Outside the liquid core, both KH and RT effects are calculated and both are considered for breakup. Typically, the RT instability grows faster when droplet acceleration is high and this effect dominates for high Weber number sprays. Mass is accumulated from the parent drop at a rate given by Eq. (17), until the shed mass is equal to 5% of the initial parcel mass. At this time, a new parcel is created with a radius given by Eq. (15).

2.6 Droplet Drag Force Models

Accurate determination of droplet drag coefficients is crucial for accurate spray modeling. Various drag models are discussed below. Many droplet drag models assume that the droplet remains spherical throughout the domain. With this assumption, the drag of a spherical object is determined by Liu et al. (1993) as

$$C_{d,sphere} = \begin{cases} 0.424 & \mathrm{Re} > 1000 \\ \dfrac{24}{\mathrm{Re}}\left(1 + \dfrac{1}{6}\mathrm{Re}^{2/3}\right) & \mathrm{Re} \le 1000 \end{cases}. \tag{22}$$

However, as an initially spherical droplet moves through a gas, its shape is distorted significantly when the Weber number is large. In the extreme case, the droplet shape will approach that of a disk. The drag of a disk, however, is significantly higher than that of a sphere. Since the droplet drag coefficient is highly dependent upon the droplet shape, a drag model that assumes the droplet is spherical is unsatisfactory. A method that dynamically determines the droplet drag coefficient considers the variations in the droplet shape. The dynamic drag model accounts for the effects of droplet distortion. It linearly varies the drag between that of a sphere and a disk. The drag coefficient is given by

$$C_d = C_{d,sphere}\left(1 + 2.632y\right), \tag{23}$$

where y is the droplet distortion. It is determined from the solution of

$$\frac{d^2y}{dt^2} = \frac{C_f}{C_b}\frac{\rho_g}{\rho_l}\frac{u^2}{r^2} - \frac{C_k\sigma}{\rho_l r^3}y - \frac{C_{dm}\mu_l}{\rho_l r^2}\frac{dy}{dt} \tag{24}$$

This equation is obtained from the TAB model of droplet breakup to calculate the droplet distortion. In the case of high Reynolds number for no distortion ($y = 0$), the drag coefficient of a sphere [i.e., 0.424 as given in Eq. (22)] will be obtained, while at maximum distortion ($y = 1$) the drag coefficient corresponding to a disk (i.e., 1.54) will be obtained.

High-Mach-number drag law (Clift et al., 1978) is similar to the spherical law with corrections to account for a particle Mach number greater than 0.4 at a particle Reynolds number greater than 20. Stokes-Cunningham drag law (Ounis et al., 1991) is for submicron particles. In this case, drag force (F_D) is defined as

$$F_D = \frac{18\mu}{\rho_p d_p^2}\frac{C_d R_e}{24}, \tag{25}$$

where R_e is the relative Reynolds number defined as

$$R_e = \frac{\rho d_p \left|\vec{u}_p - \vec{u}\right|}{\mu}$$

Here, $\vec{u}$ is the fluid phase velocity, $\vec{u}_p$ is the particle velocity, μ is the molecular viscosity of the fluid, ρ is the fluid density, ρ_p is the density of the particle, and d_p is the particle diameter.

2.7 Droplet Collision and Coalescence Model

O'Rourke's (1981) method is a stochastic estimate of collisions, which assumes that two parcels may collide only if they are located in the same continuous-phase cell. The algorithm of O'Rourke uses the concept of a collision volume to calculate the probability of collision. Rather than calculating whether or not the position of the smaller droplet center is within the collision volume, the algorithm calculates the probability of the smaller droplet being within the collision volume. It is known that the smaller droplet is somewhere within the continuous-phase cell of volume V. If there is a uniform probability of the droplet being anywhere within the cell, then the chance of the droplet being within the collision volume is the ratio of the two volumes. Thus, the probability of the collector colliding with the smaller droplet is

$$P_1 = \frac{\pi \left(r_1 + r_2\right)^2 v_{rel} \Delta t}{V} \tag{26}$$

Once it is determined that two parcels collide, the outcome of the collision must be determined. In general, the outcome tends to be coalescence if the droplets collide head-on, and bouncing if the collision is more oblique. In the reference frame being used here, the probability of coalescence can be related to the offset of the collector droplet center and the trajectory of the smaller droplet. The critical offset is a function of the collisional Weber number and the relative radii of the collector and the smaller droplet. The critical offset is calculated by O'Rourke using the expression

$$b_{crit} = \left(r_1 + r_2\right) \sqrt{\min\left(1.0\,,\, \frac{2.4f}{\mathrm{We}}\right)} \tag{27}$$

where f is a function of r_1/r_2, defined as

$$f\left(\frac{r_1}{r_2}\right) = \left(\frac{r_1}{r_2}\right)^3 - 2.4\left(\frac{r_1}{r_2}\right)^2 + 2.7\left(\frac{r_1}{r_2}\right). \tag{28}$$

The value of the actual collision parameter, b, is

$$b = \left(r_1 + r_2\right)\sqrt{Y}$$

where Y is a random number between 0 and 1. The calculated value of b is compared to b_{crit}, and if $b < b_{crit}$, the result of the collision is coalescence. The properties of the coalesced droplets are found from the basic conservation laws.

3. RESULTS AND DISCUSSIONS

Droplet breakup process in three different flow regimes, namely, (1) in quiescent atmosphere, (2) in the presence of subsonic cross–flow, and (3) in the presence of supersonic cross–flow, are simulated. The computed flow characteristics in terms of spray penetration depth and droplet distributions are compared with experimental and other theoretical results. Simulations are performed using CFX-11 (2014) with TAB, ETAB, and RD model for the quiescent atmosphere and subsonic cross-flow test cases; while the KH-RT model is used for supersonic cross-flow test cases with Fluent 14.5 (2012).

3.1 Atomization in Quiescent Atmosphere

Droplet breakup of liquid diesel in quiescent nitrogen atmosphere is considered as the first case for validation. The experimental data of Hiroyasu and Kadota (1974) is used for the present study. A 6.9 g/s liquid fuel at a pressure of 9.9 MPa is injected through a single nozzle of diameter 0.3 mm into quiescent nitrogen gas at room temperature but having higher pressure (1.1 MPa) than the ambient. The same results were used by Kim et al. (1994) for their numerical validation of droplet breakup models. The simulation is performed with the TAB and RD breakup model using CFX-11 (2014). A domain of 120 mm (axial) $\times$ 20 mm (radial) $\times$ 125.6 mm (circumferential) size is discretized with 100 $\times$ 55 $\times$ 40 grids, respectively. Figure 2 compares the spray structure for the two different breakup models at the end of 2.5 ms and qualitatively both are in good agreement with the other numerical (Kim et al., 1994) results. The computed penetration lengths with different blob sizes (20 blobs, 50 blobs) and different grids 100 $\times$ 55 $\times$ 40 and 120 $\times$ 70 $\times$ 80 are compared with experimental (Hiroyasu and Kadota, 1974) and other computational (Kim et al., 1994) results for TAB [Figs. 3(a) and 3(b)] and RD [Fig. 3(c)] breakup models. The spray penetration is defined as the largest transverse distance attained by a given spray plume. The results match well with the experimental data except towards the end where it is underpredicting the penetration by about 9%. Nonconsideration of coalescence in the present simulation is conjectured to be the cause of this deviation. Effect of blob size is seen to be marginal in penetration length prediction and results are independent of grids.

3.2 Atomization in Subsonic Cross-Flow

To study droplet breakup in subsonic cross-flow, the experimental condition of Wu et al. (1997) is simulated with TAB and ETAB models. In the experiment, a water jet of 0.5 mm diameter and velocity of 12.8, 19.3, and 29 m/s is injected upwards into an air stream of Mach numbers 0.2, 0.3, and 0.4. The density of air is 1.633 kg/m^3. These test conditions yield the momentum flux ratios of 5.3 to 59.1.

The domain used for the simulation is of 406 mm length, 125 mm width, and 75 mm height. Three different grids (Grid 1 = 400 $\times$ 75 $\times$ 60, Grid 2 = 500 $\times$ 100 $\times$ 80, and Grid 3 = 650 $\times$ 140 $\times$ 100) are employed along the length, width, and height, respectively, to study the atomization in subsonic cross-flow. It may be noted that Grid 3 is 5 times more dense than Grid 1. The results of the SMD and particle velocity as shown in Figs. 4(a) and 5(a) are almost identical for Grid 2 and Grid 3 demonstrating the grid independence of results.

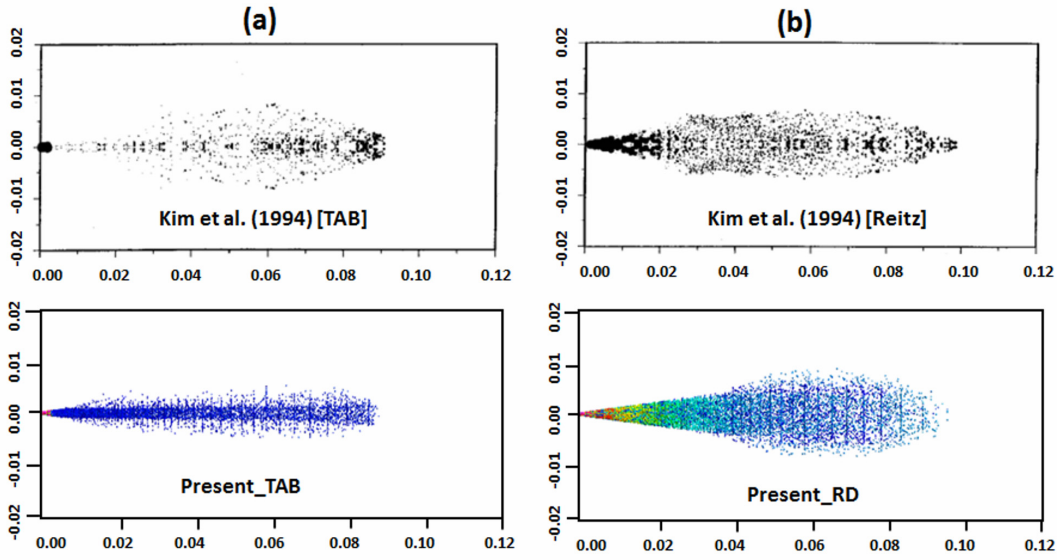

FIG. 2: Spray structure at the end of 2.5 s: (a) TAB model; (b) RD model

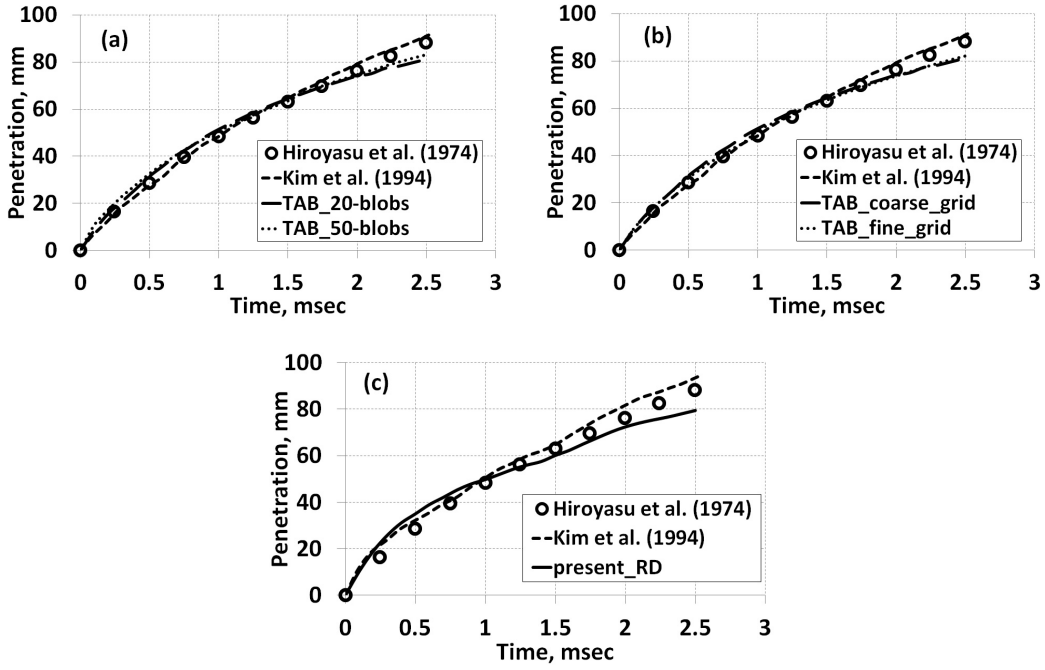

FIG. 3: Spray tip penetration vs. time: (a) effect of blob size in TAB model; (b) effect of grid in TAB model, and (c) RD model

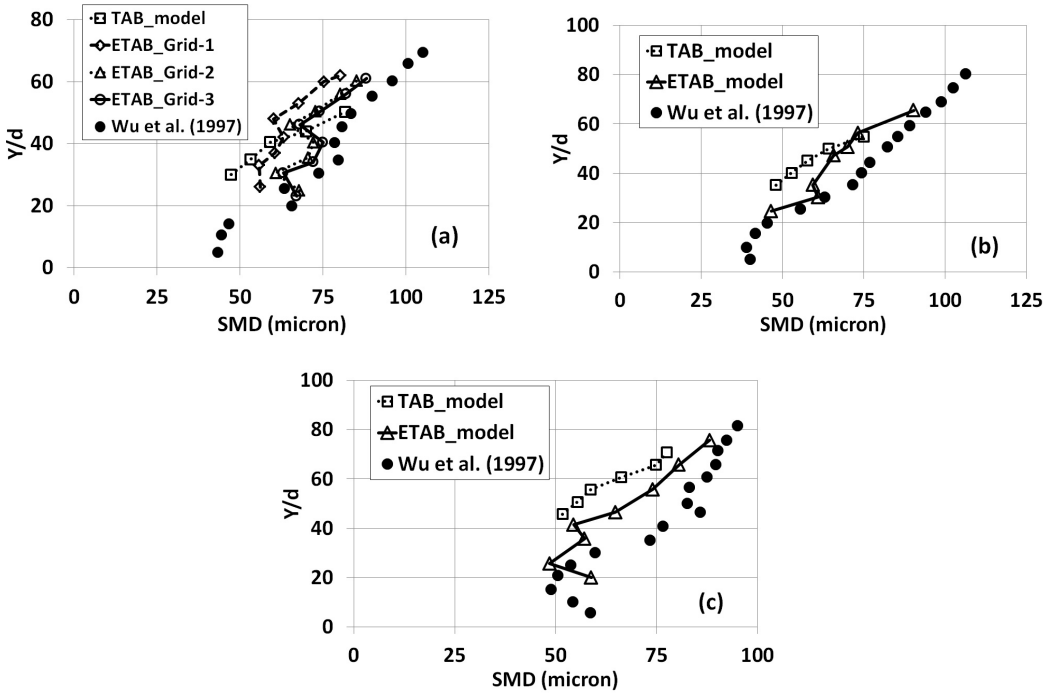

FIG. 4: Comparison of SMD distribution between experiment, TAB, and ETAB models for $Vj = 19.3$ m/s, $M = 0.3$ at different axial locations: (a) $X/d = 200$, (b) $X/d = 300$, and (c) $X/d = 500$

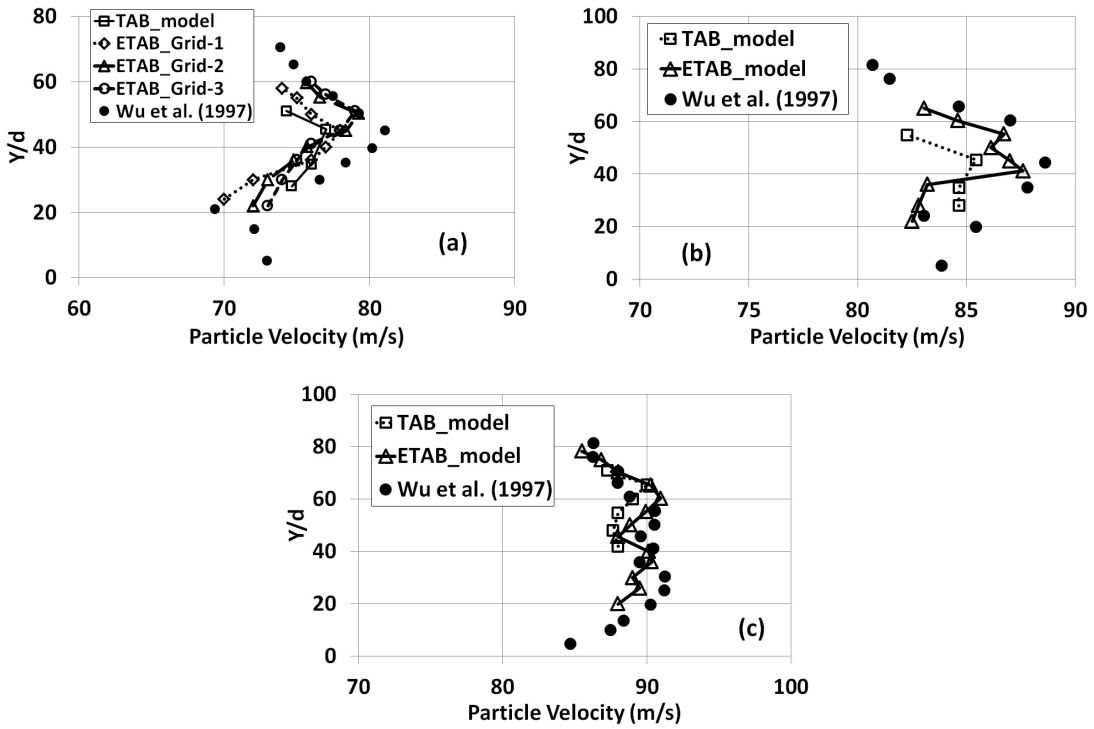

FIG. 5: Comparison of particle velocity distribution between experiment, TAB, and ETAB models for $Vj = 19.3$ m/s, $M = 0.3$ at different axial locations (a) $X/d = 200$, (b) $X/d = 300$, and (c) $X/d = 500$

The computed Sauter mean diameters (SMDs) and particle velocity of the water jet injected at $Vj = 19.3$ m/s into Mach 0.3 air flow at three axial stations of $x/d = 200$, 300, and 400 (d is orifice diameter) are compared with experimental data (Wu et al., 1997) in Figs. 4 and 5, respectively. The ETAB model has shown better prediction of spray cross section, SMD, and particle velocity compared to the TAB model.

Effect of injectant velocity on radial profile of SMD and particle velocity at $x/d = 300$ (for $M = 0.3$) is plotted in Figs. 6 and 7, respectively. The location of the spray core shifts upward and the SMD value decreases as Vj increases. Smaller droplets were observed near the bottom wall in the experiment. These droplets are generated by surface breakup and are stripped away from the periphery of the column by aerodynamic forces. The ETAB model predicts the SMD distribution better than the TAB model.

The limitation of the TAB model is that only one oscillation mode can be tracked. The droplet breakup calculations require additional information for deformation and oscillation that can be determined by Eq. (24) for the acceleration of the droplet distortion parameter. It is observed that the TAB model predicts a small ratio of child to parent droplet. This is mainly caused by the assumption that the initial deformation parameters are zero upon injection, which leads to short breakup times. The largely underestimated breakup times in turn lead to an underprediction of global spray parameters such as the penetration depth, as well as of local parameters such as the droplet size distribution. To overcome this limitation, Tanner (1997) proposed to set the initial value of the rate of droplet deformation to a negative number. The effect of setting to a negative number is to delay the first breakup of the large initial droplets and to extend their life span, which results in a more accurate prediction of spray properties.

The effect of cross-flow Mach number on SMD and particle velocity profiles at $x/d = 300$ (for $Vj = 19.3$ m/s) is shown in Figs. 8 and 9, respectively. The SMD decreases, whereas the particle velocity increases with the increase in the cross-flow air velocity. Average SMD and particle velocity (Up) were calculated across the spray cross-section plume to provide a global droplet size (SMD) and particle velocity (Up) for each test condition. Results are plotted

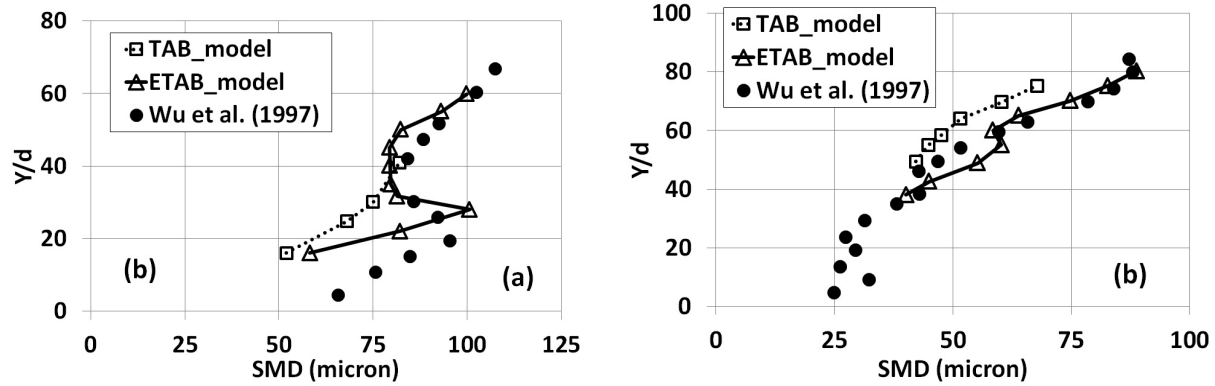

FIG. 6: Effect of injectant velocity on SMD distribution at $X/d = 300$, $M = 0.3$: (a) $Vj = 12.8$ m/s; (b) $Vj = 29$ m/s

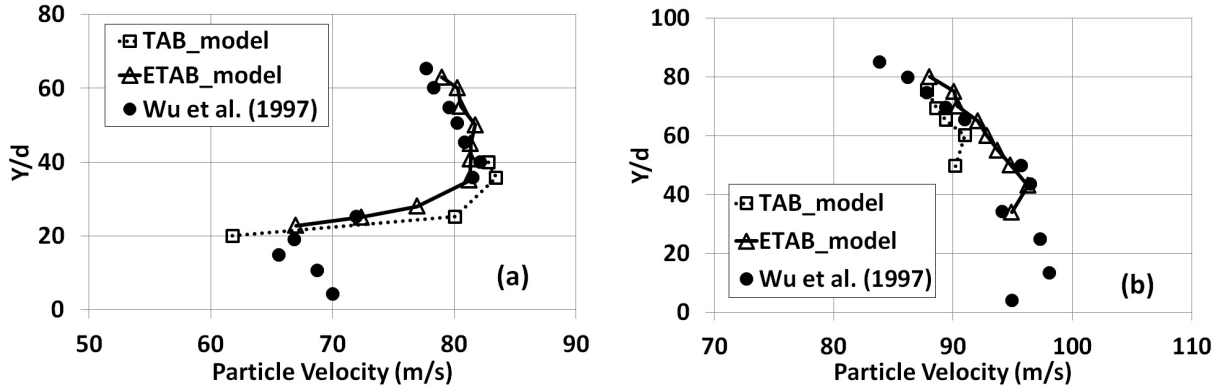

FIG. 7: Effect of injectant velocity on particle velocity distribution at $X/d = 300$, $M = 0.3$: (a) $Vj = 12.8$ m/s; (b) $Vj = 29$ m/s

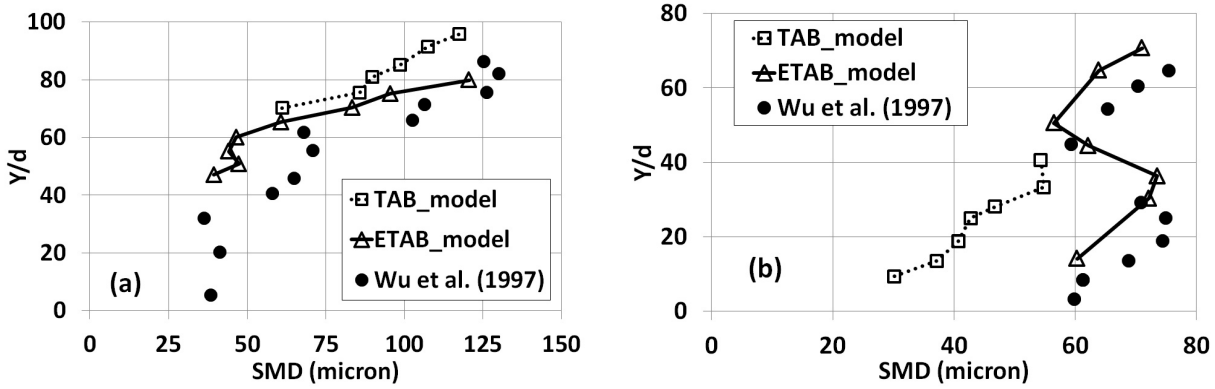

FIG. 8: Effect of cross-flow velocity on SMD distribution at $X/d = 300$, $Vj = 19.3$ m/s: (a) $u = 69$ m/s; (b) $u = 137$ m/s

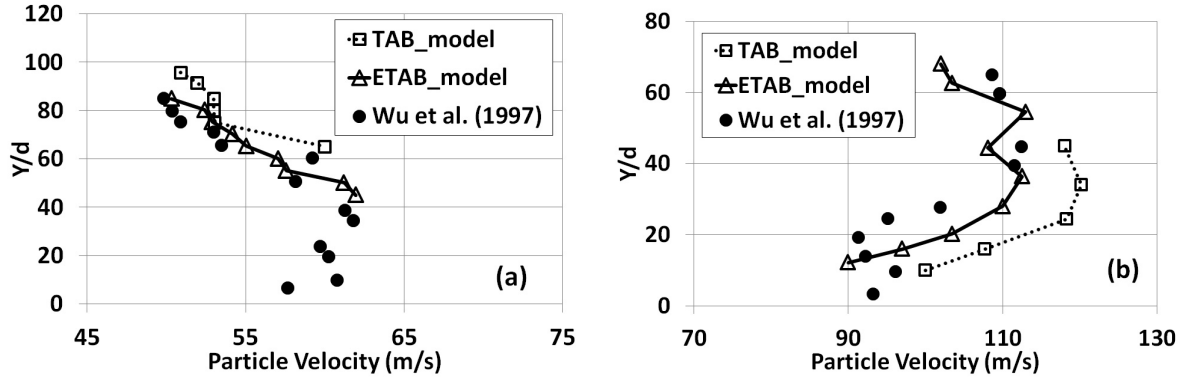

FIG. 9: Effect of cross-flow on particle velocity distribution at $X/d = 300$, $Vj = 19.3$ m/s: (a) $u = 69$ m/s; (b) $u = 137$ m/s

in Figs. 10 and 11 for different cross-flow air velocity and jet velocity, respectively. SMD was found to decrease as cross-flow velocity increases. The reduction may be explained by considering the generation of a larger number of smaller droplets because of larger momentum flux ratio and Weber number. The same is observed with increase in jet velocity. The particle velocity increases with increase in the cross-flow as well as jet velocity. This may be due to the decrease in the drop size.

The effect of the collision model in the spray characteristics is determined by simulating the atomization in the subsonic cross-flow case with and without the collision model and comparing the results in Fig. 12(a). It is observed that higher droplet collision rates are achieved in locations where relative velocity is higher. At the outer periphery of the spray, collisions result into the coalescence giving larger size droplets. A continuous increase of the droplet Sauter mean diameter is observed along the spray due to the coalescing collisions. On the contrary, for no collision, bigger droplets are observed in the central zone of the sprays, and droplet size reduces towards the periphery of the spray.

The number of blobs indicates the number of representative particles injected and tracked per unit time. Parametric studies are carried out with different blob sizes (15, 30, and 50 equals the number of blobs injected per unit mass flow rate) to study its effect in the spray behavior of the subsonic cross-flow case and the SMD profiles are compared in Fig. 12(b). The computed SMD with 30 and 50 blobs shows almost similar results; while the SMD with 15 blobs gives a smaller droplet size mainly because of a lower collision rate. For the case of 15 blobs per unit mass flow rate, the average number of representative particles is 30 with the standard deviation of 25. This number reduces as the

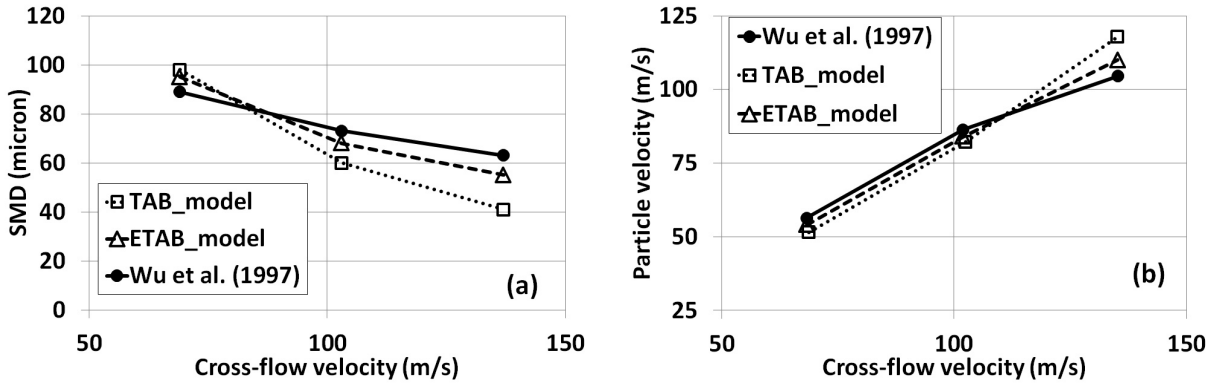

FIG. 10: Flux averaged (a) SMD and (b) particle velocity for different air velocity at $X/d = 300$, $Vj = 19.3$

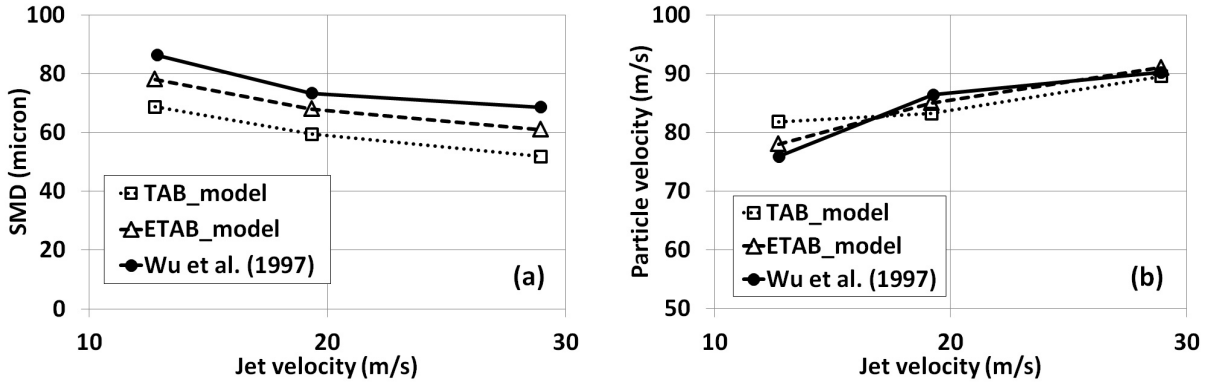

FIG. 11: Flux averaged (a) SMD and (b) particle velocity for different jet velocity at $X/d = 300$, $M = 0.3$

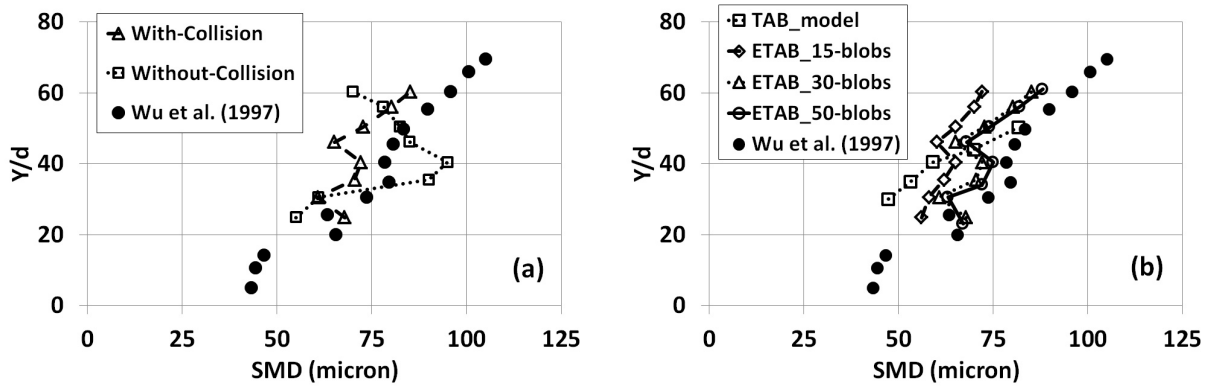

FIG. 12: Effect of (a) collision model and (b) number of blob sizes on SMD profile for subsonic cross-flow atomization

number of parcels per unit mass flow rate increases. For the case of 50 blobs, the average number of representative particles is 10 with the standard deviation of 9.

3.3 Atomization in Supersonic Cross-Flow

3.3.1 Validation Test Case 1

Yang et al. (2012) used the particle field holography (PFH) technique to experimentally investigate the spray structure very close to the injector orifice and to characterize primary atomization of liquid jets in supersonic cross-flows. Water is injected transversely through 0.5- and 0.3-mm diameter holes into a supersonic air stream of Mach 2 and 2.5 with total temperature of 300 K and variable total pressure.

The rectangular domain of 1600 mm length, 200 mm width, and 68 mm height is discretized with 1000 $\times$ 150 $\times$ 80 structured grid with good skewness and orthogonality. The grid is very fine near the wall and injector orifice with y^+ of the order $\sim$1.0. Comparison of the calculated and experimental measured droplet Sauter mean diameter for the $M = 2$ injection with 0.5 mm injector diameter and 182 kPa pressure (dynamic pressure ratio is 31) is depicted in Fig. 13. B_o is a model constant for droplet size. The higher the value of B_o, the bigger the droplets will be obtained. The predicted SMD by present simulation (with default value of $B_o = 0.61$) is higher than the experimental data. Yang et al. (2012) varied the B_o and found a better match with a value of 0.15 instead of the default value of 0.61.

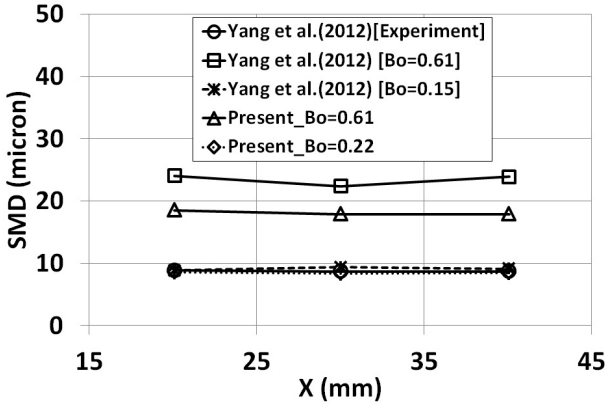

FIG. 13: Averaged SMD along axial direction for $M = 2$ injection case with 182 kPa pressure

Simulations with parametric variation of B_o revealed that a value of $B_o = 0.22$ gives a very good match of the simulation results with the experimental data. Computed spray penetration height at two different axial locations ($x/d = 50$ and $x/d = 100$) for different dynamic pressure ratios are compared with experimental data and other simulation results (Yang et al., 2012) in Fig. 14. Simulation results with $B_o = 0.22$ show a good match with the experimental results.

3.3.2 Validation Test Case 2

Experimental investigation of water injection into $M = 1.94$ cross-flow by Lin et al. (2004) is considered for the second test case of validation for atomization in supersonic cross-flow. The same problem was studied computationally by Balasubramanyam and Chen (2008) and Yang et al. (2006) for fuel atomization and combustion in a scramjet. The inlet boundary conditions of static pressure of 29 kPa, static temperature of 304.1 K, and flow velocity of 679 m/s are taken (Lin et al., 2004) for the present study. The injection velocity of the spray is determined based on jet-to-air momentum ratio of 3, 7, 10, and 15. Water is injected at a temperature of 300 K from a nozzle of diameter 0.5 mm, located at a distance of 139 mm from chamber inlet.

The computational domain is rectangular with 700 mm length, 150 mm width, and 125 mm height. Two block structured grids with $700 \times 120 \times 100$ and $740 \times 140 \times 120$ cells along the length, width, and height, respectively,

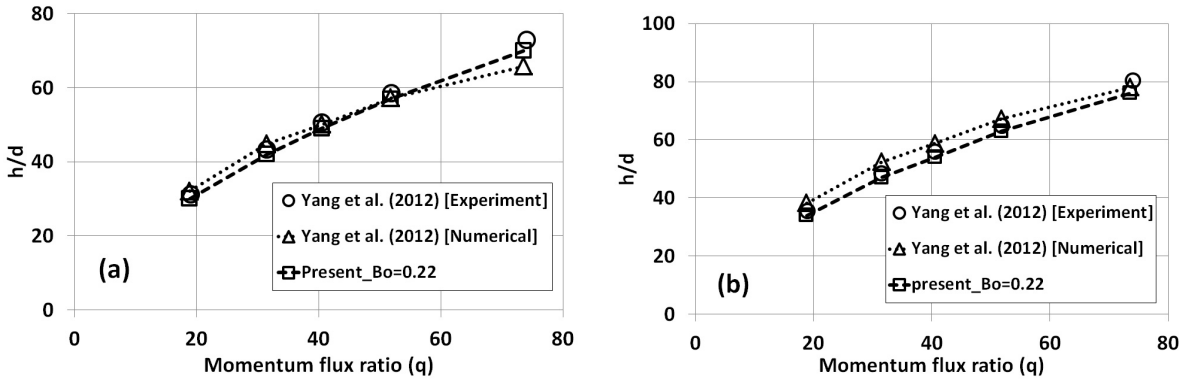

FIG. 14: Penetration length vs. momentum flux ratio at (a) $X/d = 50$; (b) $X/d = 100$

are employed to discretize the domain. The results of the SMD distribution remain unchanged for two different grids as shown in Fig. 15 which depicts the grid independence of results. The grid is very fine near the wall and injector orifice with y^+ of the order $\sim$1.0.

The computed axial distribution of spray tip penetration for the $q = 7$ case with different drag models [dynamic drag law by Liu et al. (1993), high-Mach-number drag law by Clift et al. (1978), and Stokes-Cunningham drag law by Ounis et al., (1991)] are compared with experimental data and numerical results of Balasubramanyam and Chen (2008) in Fig. 16. The jet penetration increases rapidly in the vicinity of the injector exit near the wall region and then becomes gradual due to the increase in the velocity of the air stream in the core region. The Stokes drag law matches jet penetration well with the experimental data compared to other drag models. It is to be noted that the Stokes drag model is developed for the submicron particles. In case of high-Mach drag law the particle is considered spherical and for the high Reynolds number, a fixed drag coefficient (i.e., 0.424) is obtained. The dynamic drag model calculates the droplet distortion from the TAB model, which is applicable for low Weber number flows. It overpredicts the drag force for supersonic cross-flow.

Figures 17(a) and 17(b) show the effect of various drag force models on the prediction of droplet diameter for dynamic ratios of 7 and 15, respectively. Stokes-Cunningham drag law by Ounis et al. (1991) is comparing with the experimental results in the far-field region while the high-Mach-number drag law by Clift et al. (1978) is predicting the near-field characteristics better. The computed SMD distributions for the coarse grid ($700 \times 120 \times 100$) and fine grid ($740 \times 140 \times 120$) are compared in Fig. 17(b) for Stokes drag law and the results remain unchanged for these two grids. The number of blobs for the supersonic cross-flow case is fixed based on the study of the subsonic cross-flow case. No separate studies are carried out to find out the effect of number of blobs for supersonic case. Generally,

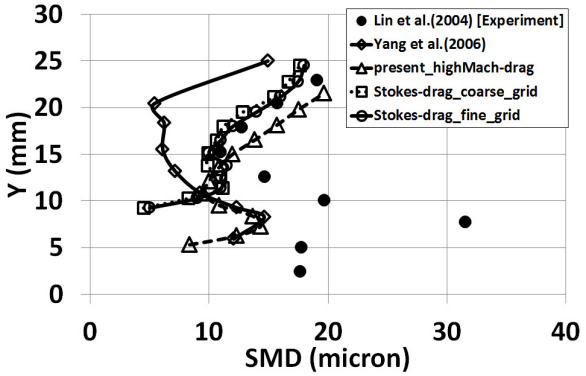

FIG. 15: Radial distribution of SMD profile for two grids at $X/d = 100$ for $q = 15$

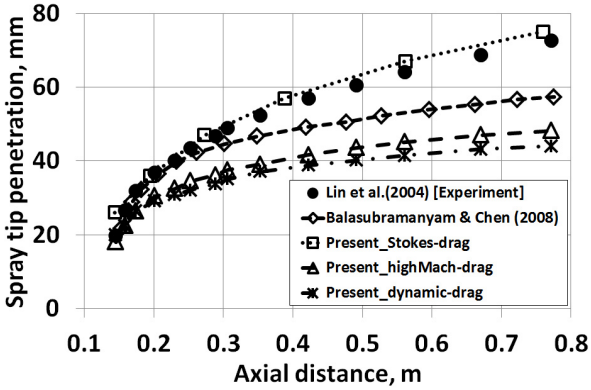

FIG. 16: Spray tip penetration for various drag force models for $q = 7$

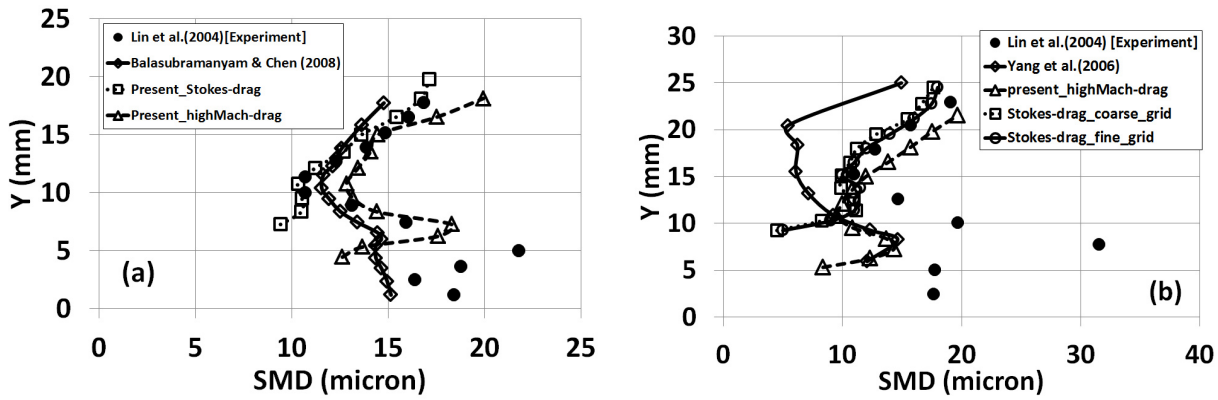

FIG. 17: Radial distribution of SMD profile at $X/d = 100$ for (a) $q = 7$; (b) $q = 15$

the droplet drag coefficient is a function of relative Reynolds number, relative Mach number, and Knudsen number. However, if the relative Reynolds number is near unity and the relative Mach number is near zero, the Knudsen number Kn becomes almost zero and the drag coefficient C_d can be expressed by the Stokes drag coefficient. The average relative particle Reynolds number observed is about 5 for the supersonic cross-flow case. The high-Mach drag law performs better for the particle Reynolds number higher than 20. It is observed that in some of the locations high-Mach drag law performs well but overall Stokes drag law has given a better SMD distribution. Further improvement in drag law to account for the high-speed effect was found to be necessary to account for supersonic acceleration of the droplets. Figure 18 shows the normalized spray tip penetration as a function of momentum flux ratio. Fairly good match (maximum difference is within 12%) is obtained between the experimental data and present simulation for the penetration height.

4. CONCLUSIONS

Various droplet breakup models available in commercial software are explored numerically to predict their capability in characterizing spray. Three-dimensional RANS equations with the K-ε turbulence model are solved using commercial CFD software. The validation test cases include liquid diesel injection into quiescent nitrogen atmosphere, subsonic cross–flow, and supersonic cross-flow of air. Grid independence of the results is demonstrated by performing simulations with different grids and comparing the results. Computed droplet velocities, droplet sizes and spray

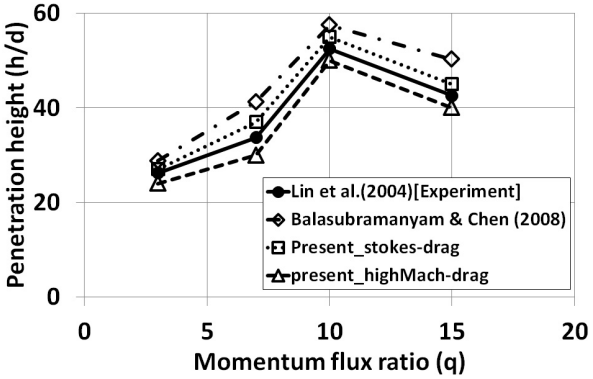

FIG. 18: Spray tip penetration vs. momentum flux ratio

structures are compared with the reported experimental/numerical data. The results of penetration match reasonably well with the experimental data for diesel injection in quiescent atmosphere. The small mismatch ($\sim$9%) towards the end may be due to nonconsideration of the coalescence/collision models. For subsonic cross-flow, it is observed that the penetration height is underpredicted, while the SMD distribution and particle velocity are matching reasonably well with the experimental data. The ETAB model predicts better spray characteristics compared to the TAB model. The effect of blob size is seen to be marginal in penetration length prediction. For droplet breakup in supersonic cross-flow, Stokes drag law matches jet penetration and radial distribution of SMD profile better with the experimental data compared to other drag models.

REFERENCES

Balasubramanyam, M.S. and Chen, C.P., Modeling liquid break-up in high speed cross flow with finite conductivity evaporation, *Int. J. Heat Mass Transfer*, vol. **51**, pp. 3896–3905, 2008.

Clift R., Grace J.R., and Weber, M.E., *Bubbles, Drops and Particles*, New York: Academic Press, 1978.

Fluent User Manual, Fluent 14.5, 2012.

Hiroyasu, H. and Kadota, T., Fuel droplet size distribution in diesel combustion chamber, *SAE Paper* no. 74-0715, 1974.

Kennedy, C.A. and Carpenter, M.H., Several new numerical methods for compressible shear layer simulation, *Appl. Numer. Math.*, vol. **14**, pp. 297–433, 1994.

Kim, Y.M., Shang, H.M., Chen, C.P., and Wang, T.S., Numerical studies on droplet breakup model, *J. Propuls. Power*, vol. **11**, no. 2, pp. 389–393, 1994.

Kitamura, Y. and Takahashi, T., Stability of liquid jet in air flow normal to the jet axis, *J. Chem. Eng. Jpn.*, vol. **9**, no. 4, pp. 282–288, 1996.

Launder, B.E. and Spalding, D.B., *Lectures in Mathematical Models of Turbulence*, London: Academic Press, 1972.

Launder, B.E. and Spalding, D.B., The numerical computation of turbulent flows, *Comput. Methods Appl. Mech. Eng.*, vol. **3**, pp. 269–289, 1974.

Levich, V.G., *Physicochemical Hydrodynamics*, Englewood Cliffs, NJ: Prentice Hall, 1962.

Lin, K.C., Kennedy, P.J., and Jackson, T.A., Structures of water jets in a Mach 1.94 supersonic cross flow, *AIAA Paper* no. 2004-0971, 2004.

Liu, A.B., Mather, D., and Reitz, R.D., Modeling the effects of drop drag and breakup on fuel sprays, *SAE Technical Paper* no. 93-0072, 1993.

Masutti, D., Bernhardt, S., Asma, C.O., and Vetrano, M.R., Experimental characterization of liquid jet atomization in Mach 6 crossflow, In *Proc. of 39th AIAA Fluid Dynamics Conference, AIAA Paper* no. 2009-4220, 2009.

Miller, R.S., Harstad, K., and Bellan, J., Evaluation of equilibrium and non-equilibrium evaporation models for many droplet gas-liquid flow simulations, *Int. J. Multiphase Flow*, vol. **24**, no. 6, pp. 1025–1055, 1998.

Nishimura, A., and Assanis, D.N., A model for primary atomization based on cavitations bubbles collapse energy, In *Proc. of ICLAS, 2000, Pasadana, CA*, July 16–20, 2000.

O'Rourke, P.J., Collective drop effects on vaporizing liquid sprays, Ph.D. Thesis, Princeton University, Princeton, NJ, 1981.

O'Rourke, P.J., and Amsden, A., TAB method for numerical calculation of spray droplet break-up, *SAE Paper* no. 8720-89, Warrendale, PA, 1987.

Ounis, H., Ahmadi, G., and McLaughlin, J.B., Brownian diffusion of submicrometer particles in the viscous sublayer, *J. Colloid Interface Sci.*, vol. **143**, no. 1, pp. 66–77, 1991.

Patterson, M.A. and Reitz, R.D., Modeling spray atomization with the Kelvin-Helmholtz/Rayleigh-Taylor hybrid model, *Atom. Sprays*, vol. **9**, pp. 623–650, 1999.

Ranz, W.E. and Marshall, W.R., Jr., Evaporation from drops, Part I and Part II, *Chem. Eng. Prog.*, vol. **48**, no. 4, pp. 173–180, 1952.

Reitz, R.D. and Diwakar, R., Structure of high-pressure fuel sprays, *SAE Technical Paper Series* no. 87-0598, 1987.

Reitz, R.D., Modeling atomization processes in high pressure vaporizing sprays, *Atom. Spray Technol.*, vol. **3**, pp. 309–337, 1987.

Sazhin S.S., Advanced models of fuel droplet heating and evaporation, *Prog. Energy Combust. Sci.*, vol. **32**, pp. 162–214, 2006.

Schetz, J.A. and Padhye, A., Penetration and breakup of liquids in subsonic airstream, *AIAA J.*, vol. **15**, no. 10, pp. 1385–1390, 1977.

Stenzler, J.N., Lee, J.G., and Santavicca, D.A., Penetration of liquid jets in a cross flow, *AIAA Paper* No. 2003-1327, 2003.

Tanner, F.X., Liquid jet atomization and drop break-up modeling of non-evaporation of diesel fuel sprays, *SAE Technical paper* 970050, 1997.

Tanner, F.X., A cascade atomization and drop break-up model for the simulation of high pressure liquid jets, *SAE Paper* no. 2003-01-1044, Warrendale, PA, 2003.

Trinh, P.H. and Chen, C.P., Development of liquid jet atomization and break up models including turbulent effects, *Atom. Sprays*, vol. **16**, pp. 907–932, 2006.

User Manual, CFX14.4, ANYSYS Inc. Products, 2012.

Wang, Y. and Rutland, C., Direct numerical simulation of turbulent droplets flow with evaporation, In *Proc. of 41st Aerospace Sciences Meeting and Exhibit*, 6–9 January, Reno, Nevada, AIAA Paper no. 2003-1281, 2003.

Wu, P.K., Kirkendall, K.A., Fuller, R.P., and Nejad, A.S., Breakup processes of liquid jets in subsonic crossflows, *J. Propuls. Power*, vol. **13**, no. 1, pp. 64–73, 1997.

Wu, P.K., Miranda, R.F., and Faeth, G.M., Effects of initial flow conditions on primary breakup of non-turbulent and turbulent round liquid jets, *Atom. Sprays*, vol. **5**, pp. 175–196, 1995.

Yang, S., Jialing, L.E., Wei, H.E., and Chen, L., Fuel atomization and droplet breakup models for numerical simulation of spray combustion in a scramjet combustor, In *Proc. of 18th AIAA/3AF International Space Planes and Hypersonic Systems and Technologies Conference, Tours, France, AIAA Paper* no. 2012-5801, 2012.

Yang, S., Jialing, L.E., Zhao, H., and Zheng, Z., Parallel numerical investigation of fuel atomization and combustion in a scramjet, In *Proc. of 14th AIAA/AHI Space Planes and Hypersonic Systems and Technologies Conference, AIAA Paper* no. 2006-8130, 2006.

Yang, S.J., Sung, H.G., and Yang, V., Large eddy simulation of break-up and atomization of a liquid column into cross turbulent flows, In *Proc. of Asia-Pacific Int. Symp. of Aerospace Technology*, Gifu, Japan, Paper no. JSASS-2009-5517, 2009.